T.3: Fiber Bragg gratings written by second harmonic of copper vapour laser

Ramakanta Mahakud

Laser Systems Engineering Section
Email: rkmahakud@rrcat.gov.in

1. Introduction:

Optical fiber Bragg gratings (FBGs) are used as critical components in fiber optic sensing, communication and fiber lasers. The FBGs are usually written by inducing permanent change in refractive index in germane-silicate fibers upon exposure to a UV fringe pattern of submicron period [1-4]. The stability and contrast of UV fringes are crucial for FBG fabrication. These parameters depend on UV source used in FBG fabrication. The low coherence sources used include excimer [KrF (248 nm), ArF (193 nm)] and femtosecond laser radiation [1-2]. The CW and high coherence sources used include frequency doubled Argon ion laser, frequency quadrupled Nd^{3+}: YLF laser, frequency doubled Krypton ion laser [1-2]. Phase mask based FBG fabrication is wavelength specific. The prism based interferometers, suitable to write FBGs at different wavelength, demands stable UV beams of high spatial and temporal coherence [5-7]. The UV radiation (255 nm) obtained from frequency doubled copper vapor laser (CVL) lies closer to 240 nm absorption band of germanium doped silica fibers.

In RRCAT, an FBG writing facility is established based on highly coherent, high repetition rate (5.6 kHz) UV pulses at 255 nm, obtained from second harmonic (SH) of copper vapor laser (CVL). This article presents analysis, fabrication and characterization of FBGs written by 255 nm UV source. The UV beams of different spatial coherence and pointing stability are employed for fast FBG fabrication in different photosensitive fibers, typically in a few minutes. Phase mask and biprism interferometers are employed. The fabricated FBGs are characterized in terms of rate of growth, saturation and spectrum bandwidth. It is analytically shown that the contrast and stability of UV fringes depend on both the UV beam parameter and the interferometer set up. The spectral evolutions of FBGs are analyzed by a physical model, based on one photon absorption. The evolution of Bragg wavelength of FBGs written in different fibers subjected to external perturbation such as strain and temperature is characterized.

2. Fiber Bragg grating (FBG) concept:

Fiber Bragg gratings are made by inducing permanent refractive index (RI) modulation in the core of an optical fiber. The fiber Bragg gratings are distinguished by their pitch, tilt and RI modulation envelope. The UV fringes induced RI distribution [$\Delta n(z)$] along *fiber axis (z) in a typical FBG* (Fig.T.3.1) *is expressed as,*

$$\Delta n(z) = <\Delta n(z)> + \Delta n_{mod}(z)\cos\{\frac{2\pi}{\Lambda(z)}z + \phi(z)\}] \quad (0 \le z \le L)$$

where $<\Delta n(z)>$, $\Delta n_{mod}(z)$, $\phi(z)$, $\Lambda(z)$ and L are average RI change, RI modulation, chirp, period and length of FBG respectively.

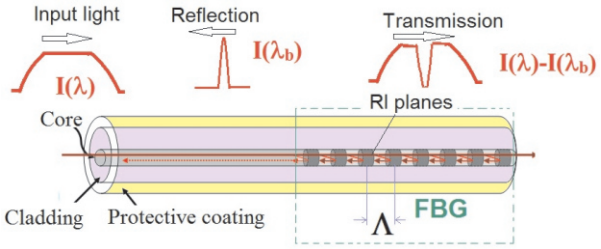

Fig.T.3.1: Schematic of a FBG structure in the fiber

The reflection at Bragg wavelength is due to coupling of counter propagating guided modes in the fiber core. In a uniform grating, the grating planes are of constant period (Λ) and normal to the fiber axis (z). The wavelength at which phase matching occurs is given as [1]

$$\lambda_b = 2\, n_{eff}\, \Lambda \qquad (2)$$

where λ_b is the Bragg wavelength, n_{eff} is the effective index of the fiber. The FBG reflectivity (R) at resonance and spectrum bandwidth ($\Delta\lambda$) are given as [1],

$$R = \tanh^2\left(\frac{\pi\eta\Delta n_{mod} L}{\lambda_b}\right) \qquad (3)$$

$$\Delta\lambda(FWHM) = \sqrt{(\Delta n_{mod}\eta / n_{eff})^2 + (\lambda_b / n_{eff} L)^2} \qquad (4)$$

where η (~0.85) is mode overlap integral. Fig.T.3.2 shows the simulated spectrum of a uniform FBG for RI modulation (Δn_{mod}) of 0.001 and FBG length (L) of 5 mm.

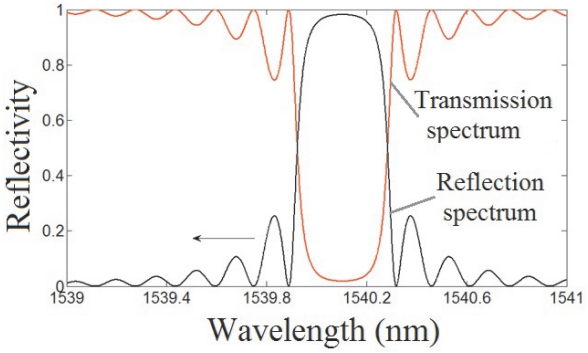

Fig. T.3.2: Simulated reflection (transmission) spectrum of a uniform FBG for Δn_{mod} = 0.001 and L = 5 mm

The transfer matrix method is used to simulate non-uniform FBG spectrum [1]. The different variants of FBG include *t*ilted, apodised and *phase-shifted Bragg gratings etc.* The Bragg wavelength (λ_b) of a FBG is susceptible to external perturbation such as strain and temperature. This is due to change in refractive index and thermal expansion of the fiber. This property is exploited for development of different types of fiber optic sensors and tuning of fiber laser.

3. CVL fundamental and its second harmonic UV beam properties:

Fig. T.3.3 shows the schematic of generation of UV beam (255 nm, 5.6 kHz, 30 ns) from frequency doubling of CVL beam. The CVL (discharge tube diameter = 28 mm, tube length = 120 cm, repetition rate = 5.6 kHz) is equipped with an unstable or spatial filtering optical resonator for higher beam quality. The CVL beam is polarized by an intra-cavity cube polarizer. The CVL beam from the oscillator was ASE filtered and then compressed (1/10 times) by suitable combination of spherical lenses (L_1 and L_2) to a diameter of about 2.8 mm for frequency conversion. The UV beam was generated from second harmonic (SH) of CVL fundamental beam (510 nm) in a β-BBO crystal, in line focusing geometry. The collimated fundamental beam was line focused by a cylindrical lens, L_3, on a β-BBO crystal (M/s Casix, 4 x 4x 7 mm cut at 51° corresponding to type-I phase matching at λ = 510nm). The fundamental and SH beams are re-collimated by a fused silica cylindrical lens, L_4, and separated by a silica prism, P.

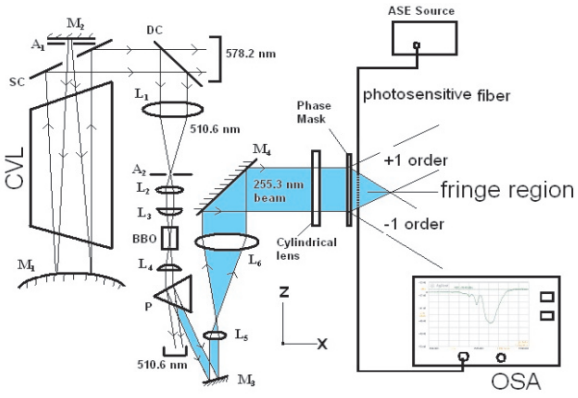

Fig.T.3.3: Schematic of CVL, SH generation and FBG fabrication by a phase mask

The UV beam parameters crucial in FBG fabrication are beam divergence, pointing stability and spectral width. These UV beam quality is guided by the fundamental CVL which in turn is controlled by its optical resonator [8-10]. Two unstable resonators of magnification 12.5 (PBUR1) and 100 (PBUR2) and a diffraction filter resonator (GDFR) are used to study the effect of UV beam characteristics on FBG fabrication. It is observed that the spatial coherence of the CVL beam improved and pulse average divergence decreased with increase in unstable resonator magnification. However, the beam quality observed for the CVL fitted with the GDFR is superior to both PBUR1 and PBUR2. The long time multi pulse far-field beam pointing and divergence fluctuations are measured over the time duration of about 10 minutes [10]. Fig.T.3.4 shows the pulse to pulse far-field divergence fluctuation. The average divergence ($\Delta\phi$) values are about 150 μrad, 110 rad and 54 rad for PBUR1, PBUR2 and GDFR CVL beams respectively.

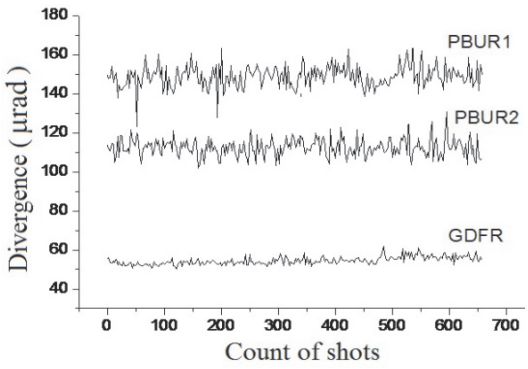

Fig. T.3.4: Pulse to pulse divergence fluctuation

The estimated maximum beam pointing instability were approximately ±22 μrad, ±11 rad, ±4 rad for PBUR1, PBUR2 and GDFR CVL beams respectively (Fig.T.3.5). The observed far-field divergence and peak intensity fluctuations are least for GDFR CVL as compared to PBUR CVLs. The UV beams generated from frequency doubling of CVL fundamental beams for PBUR1, PBUR2 and GDFR configurations are referred as UV1, UV2 and UV3 beams respectively further in the text.

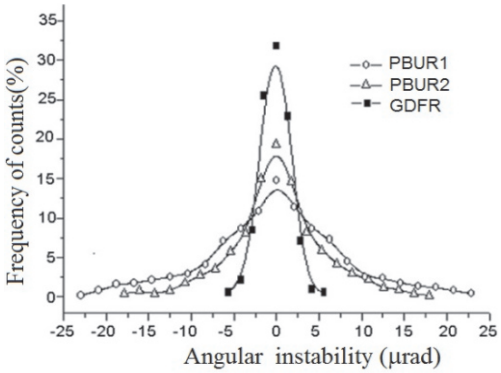

Fig. T.3.5: Probability distribution of angular beam pointing instability

The maximum UV powers obtained are about 600 mW (UV1), 650 mW (UV2) and 325 mW (UV3). The UV beam

profile is nearly top hat. The divergence of UV3 beam is diffraction limited. The collimated UV beam of diameter 2.8 mm was magnified by telescopic combination of lenses (L5 and L6 in Fig. T.3.3) to the diameter of about 10 mm. The spatial coherence was mapped by a cylindrical lens based reversible shear interferometer [7]. Fig.T.3.6(a-c) show the typical reversible shear interferometer fringes for UV1, UV2 and UV3 beams respectively.

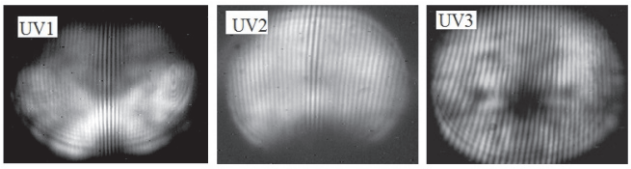

Fig.T.3.6: Reversible shear interferogram of UV1, UV2 and UV3 beams

Highest degree of coherence is observed the for UV3 beam. The spatial coherence characteristics of the SH beam (255 nm) followed the same trends as that of fundamental CVL beams. The power and UV beam characteristics are good enough to write fiber Bragg gratings.

4. FBG fabrication methods used:

Phase mask or biprism interferometers have been used to write FBGs in single mode photosensitive fibers. Fig.T.3.7 shows the photograph of FBG inscription set up established in LSES, RRCAT. A phase mask, used in transmission, is a relief grating etched in UV transmitting silica plate. The FBG are inscribed in the interference field of phase mask's +1 and -1 order diffracted beams. Zero and higher order diffraction are suppressed. The UV beam is line focused by a cylindrical lens to increase the power density on the fiber.

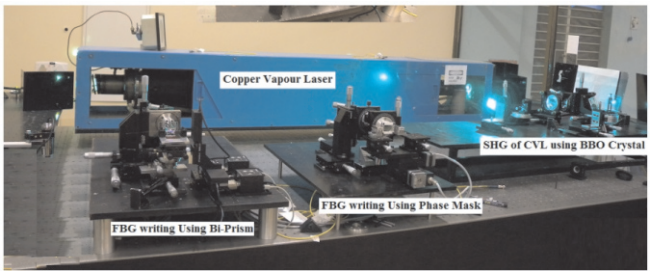

Fig.T.3.7: Photograph of CVL, UV generation and FBG inscription using a phase mask or a biprism

The FBG spectra are recorded with the help of an optical spectrum analyzer (OSA), a broadband amplified spontaneous emission (ASE) source and a three port circulator. The RI modulation is calculated from observed transmission dip of the FBG. Ge-doped and Ge-B codoped fibers are used in FBG writing. The typical fiber specifications are: core diameter ~ 7-8 μm, cladding diameter ~125 μm, coating diameter - 245 μm and cut-off wavelength ~ 1100 –1260 nm. Most of studies, focused on achieving high FBG reflectivity, were carried out using highly spatially coherent UV3 beam. The FBG writing in C-band has been carried out by a standard phase mask (Ibsen, zero order suppressed) of pitch 1060 nm. Phase mask based FBG writing is wavelength specific. A 24° refraction angle biprism with a geometrically diverging UV beam used to write FBGs at different Bragg wavelength. The evuloution of Bragg wavelength and RI modulation with temperture has been recorded by heating them in a programmable PID controller based oven.

5. UV fringe analysis:

The usable fringe area for FBG fabrication and the variation of fringe visibility in the beam overlap region are the cumulative effect of spectral and spatial frequency spectrum of the laser source, intensity distribution across the beam and stability of the fringe system. The sub-micron UV fringes used in FBG writing is difficult to resolve due to practical limitations on resolution optics. Therefore analytical studies on contrast and stability of fringes have been carried out for phase mask and biprism fringes used in FBG fabrication.

5.1 Phase mask based writing:

Fig. T.3.8 represents the schematic of UV beam (of diameter 2w) incident normally on the phase mask (of period d) in the YZ plane (x = 0). The ±1 diffraction angles (α) of the phase mask are given as, $\alpha = \pm \sin^{-1}(\lambda_{uv}/d)$. The period ($\Lambda$) of the fringe pattern is equal to half of the phase mask period i.e. = d/2. The length (L) of the FBG written at a distance x from the phase mask is given as, $L(x) = 2(w - x\tan\alpha)$.

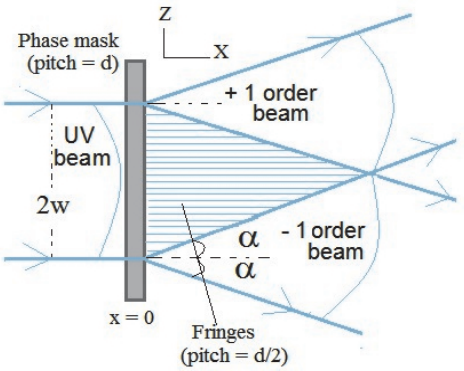

Fig. T.3.8: Schematic of overlap of +1 and -1 diffracted beam of the phase mask

The effect of UV beam spatial coherence on fringe contrast is analyzed by implicitly incorporating the far field divergence ($\Delta\phi$) as angle of incidence of set of plane waves falling on phase mask, varying within envelope of $-\Delta\phi/2$ to $\Delta\phi/2$ where $\Delta\phi$ is the diffraction divergence. The fringe visibility [γ (x)], in a fringe plane at a distance x from the phase mask, is given as [11]

$$\gamma\ (x, \Delta\phi) = |\mathrm{Sinc}\ (k_{uv} \times \Delta\phi \tan\alpha)| \qquad (5)$$

where k_{uv} ($=2\pi/\lambda_{uv}$) is the propagation constant. Fig.T.3.9 shows the fringe intensity distribution for typical values of $\Delta\phi$ = 150 µrad. The UV fringe visibility decreases with increase in distance of the fringe plane from the phase mask.

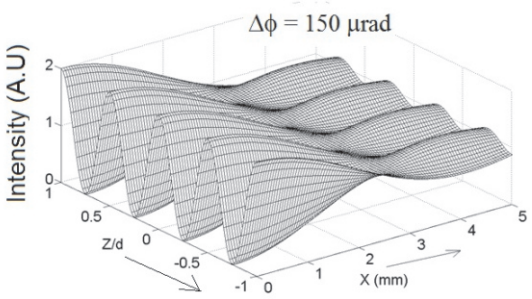

Fig. T.3.9: Fringe intensity distribution (simulated) for UV beam divergence, $\Delta\phi$ = 150 µrad and d=1060 nm

The plane (x_0) of zero fringe visibility is given as $x_0 = \sigma_{coh}/2\tan\alpha$ where σ_{coh} ($=\lambda/\Delta\phi$) *is* transverse coherence width. Fig. T.3.10 shows the variation of fringe contrast for $\Delta\phi$ = 0.062 mrad and $\Delta\phi$ = 1 mrad. The distance of FBG writing plane from the phase mask will decrease with increase in beam divergence. The visibility plot of Fig.T.3.9 is for constant divergence. However, the divergence of the CVL beam evolves within the pulse and so will be the UV pulse. Thus the single UV pulse fringe contrast is weighted average of divergence of different round trips.

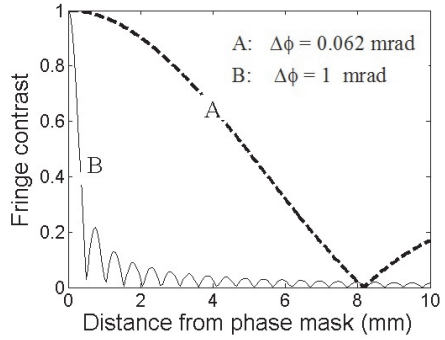

Fig. T.3.10: Variation of UV fringes contrast [$\gamma(x,\Delta\phi)$] with change in distance (x) from the phase mask

5.2 Biprism based FBG writing

The biprism divides the incident beam into two refracted beams which overlap after passing through the prism. Fig. T.3.11 shows the schematic of a collimated UV beam incident normally on the biprism of refracting angle A and material refractive index n_p. The apex of the biprism (O) is taken origin and x-axis as optical axis. The fringes modulated along z direction are produced in the rhombus shaped overlap region OPQR. The optical path lengths in the interferometer geometry are calculated by ray optics. The Bragg resonant wavelength of the FBG, written by this fringe system, is given as

$$\lambda_b = 2\ n_{eff}\ \lambda_{uv}/2\sin\alpha \qquad (6)$$

where α [$= \sin^{-1}(n_p \sin A) - A$] is half of the angle of intersection between refracted beams.

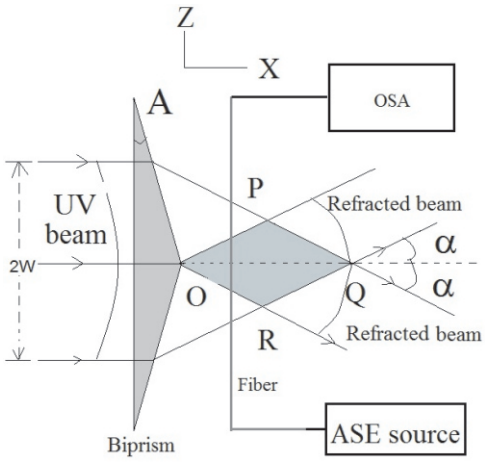

Fig. T.3.11: Biprism based FBG writing

For a narrow line width laser source, the contrast [$\gamma_{bp}(x)$] of fringes in a plane, at a distance x from the biprism can be expressed as [6]

$$\gamma_{bp}\ (x) = \mathrm{sinc}\ [k_{uv} \times \Delta\phi\eta_{bp}] \qquad (7)$$

where η_{bp} = [sinα.cosA / cos(α+A)]. The fringes visibility will decrease with increase in the beam divergence, refraction angle of the biprism and distance of the fringe plane from the biprism. The spatial variation of fringe visibility leads to spatial variation of refractive index modulation. Thus change of FBG length and fringe visibility with increase in distance from the biprism needs to be taken into account for optimization of FBG writing by a biprism interferometer. The FBG reflectivity (R) is maximised at the fiber position where the product of fringe contrast and grating length (L) is

maximum. The inscribed FBG length (L) increases as the distance of FBG writing plane from the apex of the biprism increase up to maximum overlap whereas the fringe visibility decreases (Eq.7).

Fig. T.3.12 shows the variation of [(x). L(x)] vs. x for inputs of A = 24^0, w = 6 mm, $\Delta\phi$ = 63 µrad and 33 µrad [correspond to diffraction limited divergence of 10 mm diameter uniform and Gaussian beam].

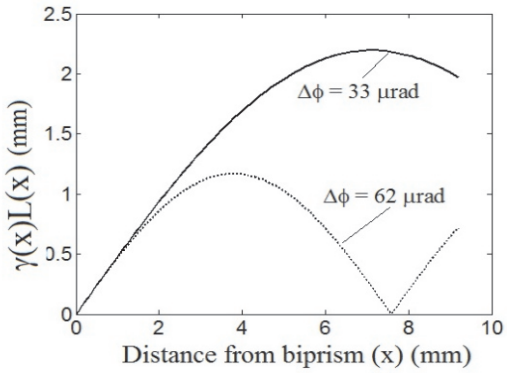

*Fig. T.3.12: Variation of [γ(x)*L(x)] with distance (x) from the apex (O) of the biprism*

Non-collimated UV beams have been used to write FBGs at different Bragg wavelength. For a symmetrically diverging/converging UV beam incidence on the biprism, the fringe width in the overlap of refracted beams changes with change in biprism to fiber distance. Fig.T.3.13 shows the change in Bragg wavelength with increase distance from the biprism for the incident UV beam geometrical divergence envelopes of $\varphi = 0^o$, 1^o and 2^o on the biprism for inputs A = 24^o, w = 5 mm, λ_{uv} = 255 nm, n_p=1.5 and prism height of 20 mm. A large tuning (~ 50 nm) is possible even with a small divergence envelope. Higher divergence envelope will lead to chirp in the FBG due th hyperbolic locus of fringes.

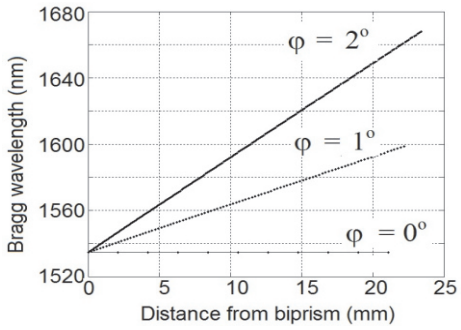

Fig. T.3.13: Bragg wavelength of an FBG written at different distance (x) from the biprism for UV beam geometrical divergence envelope (φ) of 0, 1^o and 2^o

5.3 Fringes stability:

The spatial shifting of fringes will inhibit the FBG fabrication which requires fringes of submicron period. The spatial shifting of fringes is attributed to the laser beam pointing instability which is aggregate of intrinsic laser beam dithering, mechanical vibration and environmental disturbances.

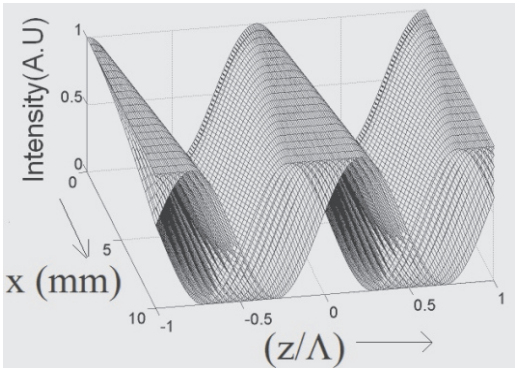

Fig. T.3.14: Shift in position of fringes in different planes (x) for pointing angle (δθ) varying between - 10 µrad to +10 µrad

The angular beam pointing instability causes pulse to pulse change in angle of incidence of the UV beam on the beam splitter (phase mask/biprism). This leads to change in direction of stratification and pitch of the fringe system because of the change of angles of diffracted (phase mask) or refracted (biprism) beams traced with the optical axis (x-axis). Detailed analysis [12] showed that fringe shift (~ xδθ) in a fringe plane (x) depends both on angular beam pointing (δθ) fluctuation and the distance (x) of the fringe plane from the beam splitter. Fig. T.3.14 shows positional fluctuation of fringes (simulated) for angular beam pointing disturbance varying between -10 µrad to + 10 µrad for Λ = 0.53 µm [12]. The fringe instability (defined as the ratio of fringe shift to fringe period) increases with decrease in the fringe period and increase in both the distance of the fringe plane from the beam splitter and angular beam pointing instability. The effect of fringe instability on biprism based FBG fabrication is higher as the FBG writing plane is comparatively at larger distance from the biprism in compared to phase mask interferometer.

6. Analysis on induced RI modulation:

The depletion of GeO defects in the core of germano-silica fiber upon UV illumination triggers formation of trapped states (defect induced defects). The subsequent structural change attributed to cumulative effect of color-center, compaction and photo-elastic effects lead to change in

refractive index the fiber core [1]. The absorption of 255 nm radiation by GeO defects is of one photon in nature due to low intensity (~ 0.1 MW/cm^2). Based on one photon absorption, the UV fringes induced refractive index is described as [11],

$$\Delta n_n(z) = \frac{\Delta n(z)}{\Delta n_{max}} = 1 - \exp[-\beta F_0 (1 + \gamma \cos \frac{2\pi}{\Lambda} z)] \quad (8)$$

Where Δn_{max} is saturable index change, $\beta[= \sigma(v)/hv_{uv}, \sigma$ - absorption cross section], γ is fringe contrast and $F_0[= NI_0\tau$; N is number of pulses, I_0 is fringes mean intensity and τ is pulse duration] is the accumulated mean fluence. The terms $\Delta n_n(z)$ and βF_0 are described as normalised RI change and normalised fluence respectively.

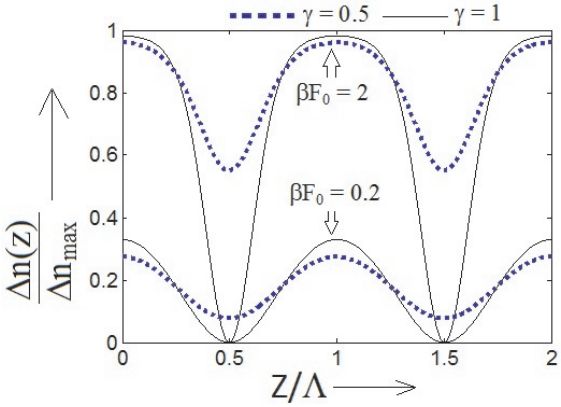

Fig. T.3.15: Spatial distribution of $[\Delta n(z)/\Delta n_{max}]$ at low and high fluence for $\gamma(x) = 1$ (ideal), $\gamma(x) = 0.5$

Fig. T.3.15 shows the distribution of normalised RI change $[\Delta n(z)/\Delta n_{max}]$ at normalized fluence of 0.2 and 2 (simulated for $\beta = 0.001$ cm^2/J) for fringes of high ($\gamma = 1$) and low ($\gamma = 0.5$) contrast. The spatial distribution of $\Delta n_n(z)$ changes with fluence and fringe contrast. The UV fringes induced RI distribution which is sinusoidal at low fluence deviates from sinusoidal with increase in accumulated fluence. The nor. RI change expressed in Fourier is given as ,

$$\Delta n_n(z) = \Delta n_n^{(0)} + \sum_m \Delta n_n^{(m)} \cos \frac{2m\pi}{z} \quad (9)$$

where $\Delta n_n^{(m)}$ is the amplitude of mth harmonic component of induced RI and $\Delta n_n^{(0)}$ is change in average RI. The first harmonic component $[\Delta n_n^{(1)}]$ and zero (dc) component $[\Delta n_n^{(0)}]$ of $\Delta n(z)$ contributes to FBG reflection at Bragg wavelength and Bragg wavelength shift during FBG inscription respectively. Fig. T.3.16 shows the evolution of $\Delta n_n^{(0)}$ and $\Delta n_n^{(1)}$ with fluence (simulated for $\beta = 0.001, \gamma = 0.5$ and 1).

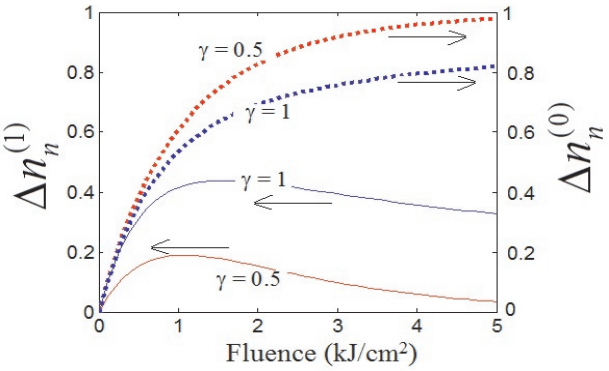

Fig. T.3.16: Simulated evolution of $\Delta n_n^{(0)}$, $\Delta n_n^{(1)}$ with Fn_0 for $\gamma = 0.5$ and $\gamma = 1$

The growth and saturation of of RI modulation [$= \eta\Delta n_{max}$ x $\Delta n_n^{(1)}$] is higher for fringes of higher contrast (γ). The change of FBG reflectivity and Bragg wavelength shift with increase in accumulated fluence during inscription is shown in Fig. T.3.17. The simulated FBG reflectivity decreased after saturation due to decrease in RI modulation. The FBG spectrum bandwidth will first increase to maximum (at saturation) and than decrease (due to decrease in RI modulation) with increase in accumulated fluence.

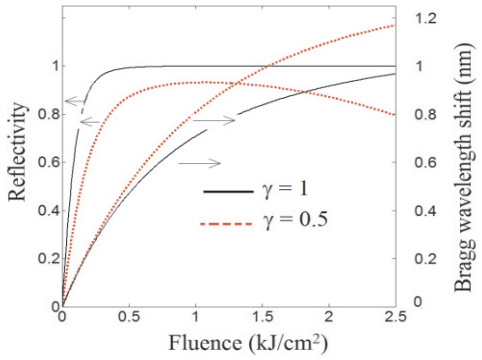

Fig. T.3.17: Change of reflectivity and Bragg resonant wavelength shift with accumulated fluence simulated for $\Delta n_{max} = 0.001$, $L = 5$ mm, $\lambda_b = 1540$ nm

6.1 Effect of UV beam profile on growth of FBG reflection spectrum:

The induced RI modulation is uniform along FBG length for a uniform fringe pattern. However for a cylindrically focussed Gaussian or top hat UV beam, the fringe intensity envelope in a particular fring plane (x) is non uniform [13]. This nonuniformity is also different for different fringe planes. Therefore the saturation of RI modulation at different

sections of the FBG will occur at different exposure times. Also with continuous exposure of UV fringes, the RI modulation envelope along FBG length will dynamically change due to nonlinear growth of photo-induced refractive index [11]. The dynamic the evolution of RI modulation envelope will affect the evolution of FBG reflection spectrum during inscription [13].

As an illustration, Fig. T.3.18 shows simulated evolution RI modulation with increase in normalised fluence (βF_0) at a distance (x) of 2 mm from the phase mask for a cylindricall focussed Gaussian beam of diameter 10 mm. At low fluence, the RI modulation enevelope is tappered, akin to the fringe intensity envelope. With increase in accumulated fluence, it approaches flatter. With further increase in exposure, the dip at the centre appears due to saturation at the in the centre of fringe intensity envelope where intensity is higher. The reflection spectrum of a FBG have side lobes on both sides of the Bragg resonant wavelength where as the reflection spectrum is apodised for a Gaussian RI modulation envelope [13].

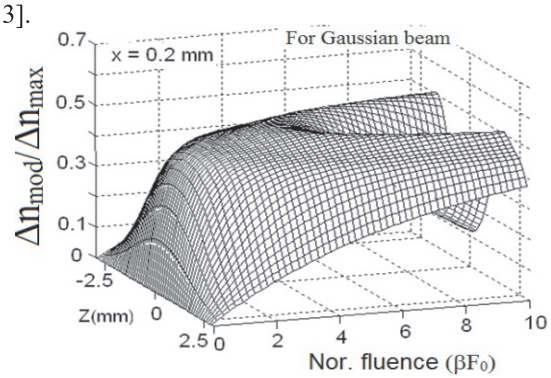

Fig. T.3.18: Evolution RI modulation envelope

7. Results and discussion:

7.1 FBG fabrication by phase mask:

7.1.1 FBG growth characteristics:

During continuous exposure of UV fringes, the FBG reflectivity grew to saturation. Fig. T. 3.19 shows the transmission spectrum of a FBG at different fluence.

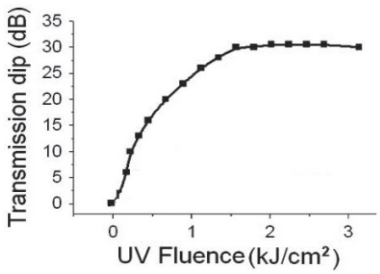

Fig. T.3.19: Change in transmission dip of a FBG with increase in accumuled fluence

Fig. T.3.20 shows the change in transmission dip of a FBG with fringe exposure time. The growth rate is initially steep and gradually approached zero at saturation. The traces marked as 1, 2, 3 and 4 corresponds to fluence of 0.1 kJ/cm^2, 0.5 kJ/cm^2, 1 kJ/cm^2 and 2 kJ/cm^2 respectively. The Bragg resonant wavelength shifted towards red due to increase in average RI. The spectrum bandwidth increased due to increase in RI modulation. The estimated RI modulation contrast reduced with growth of FBG reflectivity. The reflection spectrum evolved with change in the structure and strength of side lobes. The side lobes on the blue side of the spectrum appeared first. The saturated FBGs have side lobes on both side of the spectrum. The observed results on the spectrum matched with the analysis [12-13].

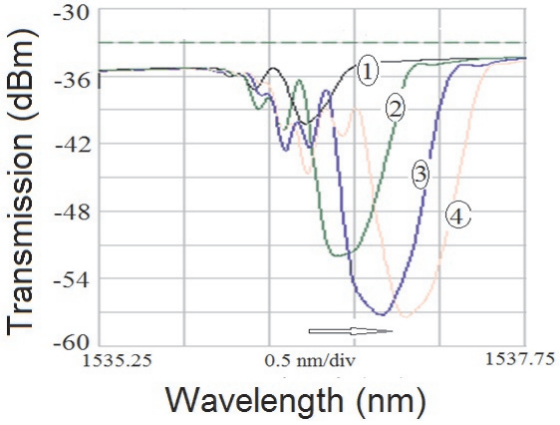

Fig. T.3.20: Transmission spectrum of a FBG at different accumulated fluence

The reflectivity of FBGs written at higher phase mask to fiber distance decreased. This is due to decrease in both FBG length and fringe contrast. The FBG relectivity reduced with decrease in FBG length.

7.1.2 Effect of UV beam quality

For a comparative study on effect of spatial cohernce and beam pointing instability on FBG fabrication, UV1, UV2 and UV3 beams of diameter 10 mm has been used to write type I FBGs by a phase mask of pitch 1060 nm. The growth rate and saturation of RI modulation is higher for FBGs written by UV beams of higher spatial coherence. This is due to higher contrast and stability of fringes at the FBG writing position for UV beams of higher spatial coherence.

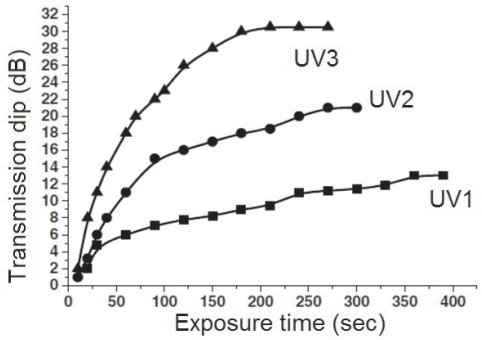

Fig. T.3.21: Growth of transmission dip of FBGs written by UV1, UV2 and UV3 beams with exposure time

The UV power (220 mW), phase mask to fiber distance (0.8 mm) and photosensitive fiber (PS-RMS-50, core dopants: B_2O_3 and GeO_2) are same [12]. Fig. T.3.21 shows the growth of transmission dip of FBGs with fringe exposure time. The maximum transmission dip of FBGs written by UV1, UV2 and UV3 beams are about 13 dB, 21 dB and 32.5 dB respectively. The Bragg wavelength shifted by about 0.7 nm during FBG inscription due to increase in photoinduced average refractive index. The RI modulation increased non-linearly to saturation at different rate for different UV beams.The saturated value of RI modulation (Δn_{mod}) estimated from observed maximum transmission dip (T_d) are 1.25 x10^{-4}, 1.75 x10^{-4} and 2.37 x10^{-4} for FBGs written by UV1, UV2 and UV3 beams respectively. Thus it is established the fact that fringe contrast which is controlled by spatial coherence and pointing stability of the CVL-UV beam predominantly controlls the FBG fabrication efficiency. The trends of the experimental results are in tune with the analysis [12].

7.1.3 Effect of fiber composition:

FBGs have been written in different photosensitive fibers [14-16]. Table 1 shows the maximum observed transmission dip (reflectivity) of FBGs in different fibers written by UV3 beam.

Table-1: Reflectivity of FBGs in different fibers

Fiber (Core doping)	T_d (dB), (Reflectivity)
PS-270 (CGCRI) Ge-8 mol %,B- 6 mol %	38 (99.98%)
SM-1500(Fiber core) Ge- mol 18%	32 (99.94 %)
NM-113(CGCRI) Ge-10 mol %	30 (99.9 %)
GF-1(Neufern) Ge-B codoped	30 (99.9 %)
CMS-1550-R1 (Stocker Yale) Ge doped	26 (99.74 %)
PS RMS 50 Stocker Yale Ge- B codoped	30.5 (99.91 %)
SMF 28 Ge – 3 mol %	0.5 (10.8 %)

The observed growth and saturation of refractive index modulation, Bragg wavelength, bandwidth and saturation fluence required are different for FBGs in different fibers. This is due to difference in doping composition and molar concentration. The maximum transmission dip of 38 dB so far observed for a FBG written in fiber PS-270 (Fig. T.3.22) fiber.

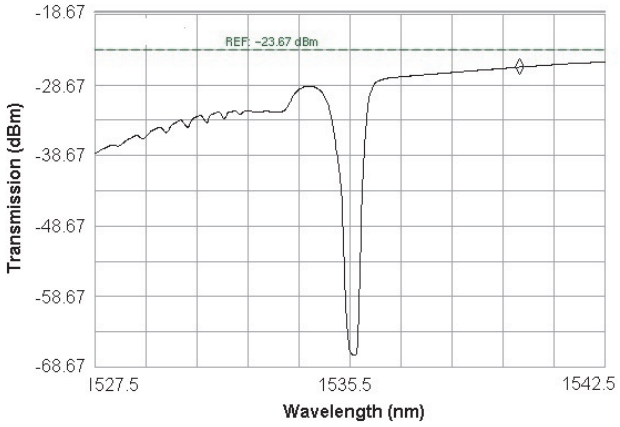

Fig. T.3.22: Transmission spectrum of an FBG written in PS-270 fiber

7.1.4 Type II A gratings:

The prolonged exposure of fringes resulted in the partial or complete erasure of type I FBG, followed by growth of a new spectral formation at much higher fluence, known as a type IIA [14-15]. Fig. T.3.23 shows the variation of RI modulation with accumulated fluence of typical FBGs in NM 113 and SM 1500 fibers. Type IIA FBG growth started at much higher fluence of 15 kJ/cm^2 and 24 kJ/cm^2 for SM1550 and NM113 fibers respectively. The type IIA growth is attributed to stress relaxation in the fiber core.

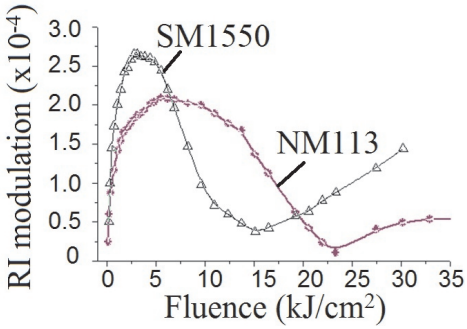

Fig.T.3.23: Variation of RI modulation with accumulated fluence

7.1.5 Tilted Bragg gratings:

The grating normal is inclined with fiber axis in a tilted FBG. The tilted FBGs have been written by rotating the phase mask in the vertical plane [16]. Fig. T.3.24 shows the transmission spectra of a tilted FBG written in a single-mode fiber (PS 270).

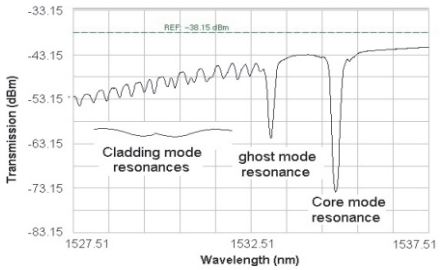

Fig. T.3.24: Transmission spectrum of a tilt FBG

The resonance dips in the shorter wavelength side of the Bragg wavelength are cladding modes excited by scattering light from the core into the cladding. The Bragg resonant wavelength shifted to longer wavelength with increase in tilt angle. Fig. T.3.25 shows the reflection spectrum of array of gratings written at different tilt angles. The cladding modes do not appear in reflection spectrum. The reflectivity decreased with increase in tilt angle due to decrease in coupling coefficient.

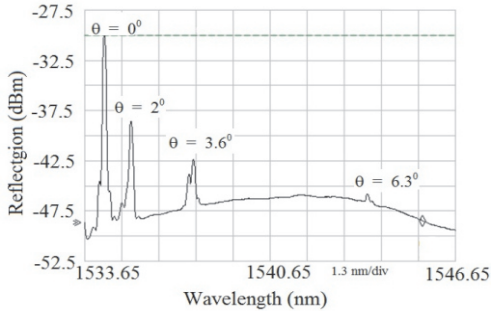

Fig. T.3.25: Reflection spectra tilt FBG array

7. 2 FBG fabrication by biprism interferometer:

In this technique, the FBG writing plane is optimised by writing FBGs at different distance from the apex of a 24° silica biprism [6]. The maximum reflectivity observed for FBG written by UV3 beam in GF1 fiber is 93.7 % (T_d~12 dB) and that in PS270 fiber is 90 % (T_d~10 dB). The maximum observed reflectivity so far is 99.8 % (T_d~ 28 dB) for FBGs in hydrogen loaded SMF-28 fiber [17-18].

A geometrically diverging UV beam is used to write FBGs at different Bragg wavelengths. Fig. T.3.26 shows the reflection spectra of three FBGs in the same fiber, marked as G_1, G_2 and G_3, written at distance (x) of 2 mm, 5 mm and 7.5 mm from the biprism respectively [6]. In this case, the UV beam was slightly diverging (~ 0.5°). The observed reflection power of the FBG written at x = 5 mm was higher due to higher value of [γ(x).L(x)].

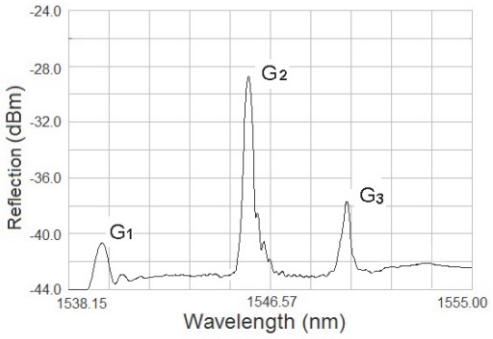

Fig. T.3.26: Reflection spectrum of FBGs written at distance from biprism

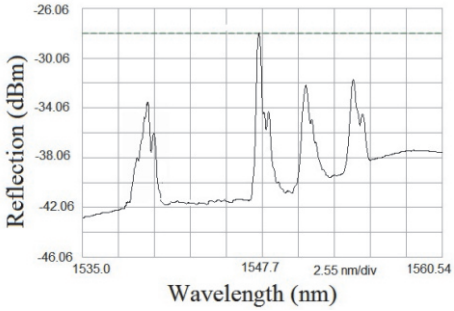

Fig. T.3.27: Reflection spectrum of FBG arrays written the collimating lens

Fig. T.3.27 shows the reflection spectrum of FBG arrays, written at distance of 5 mm from the biprism while the geometrical divergence of incident UV beam was changed.

8. Effect of temperature and strain on evolution of Bragg wavelength:

The Bragg wavelength of a FBG is sensitive to external peturbation such as temperature and strain. The Bragg

wavelength shift with temperture and strain were studied for FBGs in different fibers [19]. For a typical FBG, The strain sensitivity is about 1.2 pm/. However, the observed evolution of Bragg wavelength with temperature is quadratic and the temperature coefficients are dependent on fiber composition [19].

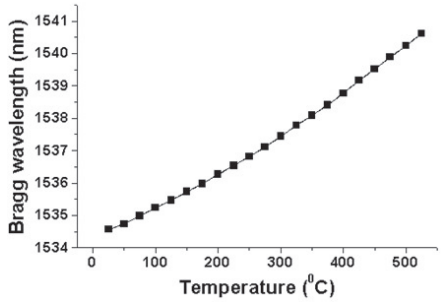

Fig. T.3.28: Variation of Bragg wavelength with temperature

Fig. T.3.28 shows the Bragg wavelength [(T)] with temperature (FBG in SM1500 fiber). The average temperature sensitivity increased from 10 pm/°C to 13 pm/°C with increase in temperature from 30 °C to 530 °C. The theoretical analysis shows that the increase in temperature sensitivity of bare FBG at elevated temperature depends mainly on second derivative of refractive index [$d^2n/dT^2 \sim 1.46x10^{-8}/(C)^2$] and thermal expansion of the fiber material [19]. The non-uniformity of temperature sensitivities of embedded FBG sensors additionally depends on strain transfer from substrate to FBG [19]. At elevated temperature, the RI modulation of FBGs decayed due to thermal relaxation. The experiments on thermal sutainability showed that the FBGs in Ge-doped and Ge-B codoped fiber could survive the temperature up to 800 C and 600 C respectively.

9. Conclusion

The analysis and experiment on FBG fabrication by frequency doubled CVL showed that growth, saturation and spectrum profile of the FBG depends on UV beam coherence, fringe stability, fiber photosensitivity and interfrometer set up. FBG growth rate is faster for high spatial coherent and stable UV beam. The FBG spectrum depends on UV beam profile and changes with increase in FBG reflectivity. The observed experimental results are in tune with the analysis. The FBG fabrication efficiency observed is lower for biprism based writing. However, high reflectivity FBGs were inscribed by suitably choosing the FBG writing plane where the product of fringe contrast and FBG is maximum. Additionally, a biprism has been used to write FBGs at different wavelength, necessary as a sensing element in distrubuted sensing. Inscribed FBGs have been utilised as temperature and refractive index sensors.

Acknowledgements:

This work is carried out mainly as a part of author's Ph.D. thesis work under guidance of Dr. S. K. Dixit, RRCAT, Indore. The author is grateful to Shri S. V. Nakhe, Head, L.S.E.S., for his support and encouragement. The author expresses gratitude to all the colleagues in the group for their valuable inputs during the course of the work.

References:

1. R. Kashyap, Fiber Bragg Gratings, Academic Press, New York, (2012)
2. K. O. Hill and G.Meltz, J. of Light wave Technology 15, 1263 (1999)
3. G. Meltz, W. W. Morey and W. H. Glenn, Opt. Lett. 14, 823 (1989)
4. A. Othonos, Rev. Sci. Instrum. 68, 4309 (1997)
5. N.H. Rizvi, M. C. Gower, Appl. Phys. Lett. 67, 739 (1995)
6. R. Mahakud, J. Kumar, O. Prakash, S. K. Dixit, *Opt. Engg.* 52, 0761141 (2013)
7. O. Prakash, R. Mahakud and S.K. Dixit, *Opt. Engg.* 50, 114201 (2011).
8. S. K. Dixit, J.K. Mittal, B. Singh, P. Saxena, R. Bhatnagar, Opt. Commun. 98, 91, (1993)
9. D. Coutts, IEEE J. Quant. Electr., 31, 330 (1995).
10. S. K. Dixit, O. Prakash, R. Biswal, J. K. Mittal, *Optics Commun* 281, 2590 *(* 2008)
11. R. Mahakud, O. Prakash, S.V. Nakhe and S. K. Dixit, Appl. *Opt* 51, 1828 *(* 2012)
12. R. Mahakud, O. Prakash, S.K. Dixit and J.K. Mittal, Opt. *Commun.* 282, 2204 (2009)
13. R. Mahakud, O. Prakash, J. Kumar, S. V. Nakhe, S. K. Dixit, *Opt. Commun.* 285, 5351 *(*2012)
14. J. Kumar, R. Mahakud, A. Mokhariwale, O. Prakash, S. K. Dixit and S. V. Nakhe, *Opt. Commun. 320, 109 (2014)*
15. J. Kumar, O. Prakash, R. Mahakud, *S. Agrawal* S. K. Dixit , S. V. Nakhe, *Opti. Engg. 53, 1171031, (2014)*
16. *O. Prakash, J. Kumar, R. Mahakud, U. Kumbhakar, S.V. Nakhe, S.K Dixit, Pramana, J. of Physics, 82, 255 (2014)*
17. *R. Mahakud, J. Kumar, O. Prakash, S. K. Dixit, S. V. Nakhe, Applied physics:B(accepted)*
18. R. Mahakud, J. Kumar, O. Prakash, S.K. Dixit and S. V. Nakhe, OSA Technical Digest (online, Jan 2015)
19. R. Mahakud, J. Kumar, O. Prakash and S. K. Dixit, Appl. *Opt. 52, 7570 (2013)*